Physics Bachelor's Thesis

Modeling coarse grained time-resolved fluorescence-detected 2D electronic spectroscopy (F-2DES)

First Examiner & Supervisor:
Thomas la Cour Jansen, Prof

Author:
Eduard Mrug S5749956

Second Examiner:
Richard M. Hildner, Prof

Supervisor:
Stephanie González-Migoni, MSc

Faculty of Science and Engineering
University of Groningen
Groningen, the Netherlands
2026

Abstract

Fluorescence-detected Two-Dimensional Electronic spectroscopy (F-2DES) is used to study energy transfer dynamics in molecular systems, enabling background-free detection with a potential for single-molecule resolution. It results in Two-Dimensional (2D) spectra showing correlations between two laser pulse excitation frequencies. Such spectra for a range of waiting times t_2 describe the system dynamics. However, the most important features of the F-2DES 2D spectra, the cross-peaks, are obscured by the dominant Exciton-Exciton Annihilation (EEA) signal. In this thesis, we used simulation of a well studied LH2 (Light Harvesting complex 2 of *R. acidophilus* system and found that decreasing the detection time t_4 improves the contrast in the 2D spectral evolution. However this effect was only significant once t_4 approached EEA timescales, here 0.1 ps. Besides experimental limitations on detection window length, this was at the cost of absolute signal strength, necessitating optimization of t_4 in experimental settings. We also devised a novel experiment, where t_2 is fixed (here at 0 fs) and a t_4-dependent signal is measured. Simulating such experiment retrieved the inherent fluorescent timescale $\tau^F = 986$ ps, while normalizing the spectra by one of the peak intensities produced plots containing EEA and exciton transfer dynamics information. The inherent simulation parameters for annihilation and transfer were varied to find their influence on these plots. While a one-to-one readout of the inherent parameters is out of reach for now, the behaviours are aligned with the known energy transfer from outer B800 to inner B850 chromophore rings. This lays the groundwork for future explorations of more inherent parameter effects and more complex fitting in pursuit of recovering the dynamics from an F-2DES experiment without prior knowledge.

Acknowledgments

I want to sincerely thank my supervisors, Prof. Thomas la Cour Jansen and Stephanie González Migoni, MSc, for their support, engagement in curiosity-driven discussions, and welcoming atmosphere in the research group. I thank Prof. Richard M. Hildner for his time and feedback on my work.

I also thank the Center for Information Technology of the University of Groningen for providing access to the Hábrók high-performance computing cluster.

A big thank you to my parents and family for making my studies here possible, supporting me throughout the erratic adventure, wishing me all the best, and checking in on me regularly. Ďakujem!

Last but not least, I thank my friends who made Groningen a home and perhaps Person an eduard: Alexandros, Danika, Ege, Irena, Kalle, Lucas, Markuss, Răzvan, Stanislavs, Toms, Viesturs, Zdeni...

And those who made Singapore a home away from home and Eduard a person away from eduard: Aoi, Adrian, Birgit, Daigo, Jacky, John, Kalle (the same one), Kiko, Lena, Sophia...

For maintaining my focus, thank you to Chopin and Rachmaninoff and those who run their codes. And to The Get Up Kids, Modern Baseball, the peggies, and empty parking lot, even if no one will run their codes again.

Not every victory enables simple xenophilia. Instead, search on! Perhaps everything person estranged explains him. As mind calibrates, leave former process. Next is rest, then we improv. Be persons, apex alumni limits!

Generative Artificial Intelligence (GenAI) usage declaration

GenAI was used for coding assistance, searching for and formatting references, and brainstorming. No AI summary was used for references. No text in this thesis is AI-generated. The models used were Gemini 3.1 Pro and Gemini 3.5-Flash from Google.

Contents

Abstract **1**

Contents **3**

1 Introduction **4**

2 Theory & Simulation Methods **6**
2.1 2D Electronic Spectroscopy (2DES) overview 6
2.2 Fluorescence detected 2DES (F-2DES) 6
2.3 Non-linear response 7
2.4 Coarse-Grained exciton model of LH2 7
2.5 Response function 8
2.6 Quantum yield time evolution 9

3 Results & Discussion **13**
3.1 F-2DES with finite t_4 13
3.2 Time (t_4) evolution of the Fluorescence-detected 2D spectrum 15
3.3 Evolution dependence on empirical parameters 16
3.3.1 Upper Cross-peak 16
3.3.2 Lower Cross-peak 17
3.3.3 Lower Diagonal peak 18
3.4 Evolution dependence on Rate matrix K 20
3.5 Limitations and future considerations 23
3.5.1 General limitations 23
3.5.2 Finite t_4 F-2DES 23
3.5.3 Parameter variation impact on experiment 23
3.5.4 UD normalization and the fitting model 24

4 Conclusions **25**

Bibliography **27**

1 Introduction

Scientists have always been studying nature at all scales accessible to their tools at the time. From watching animal behavior with our bare eyes, through expanding our vision to bacterial movements using microscopes, we have reached a point of studying the dynamics of molecular systems through means devoid of our eyes altogether. However, we still make use of light, since photons at the right frequency have the energy necessary to de/excite a molecule from one state to another. Radiation in the infrared range corresponds to vibrational state transitions, while Ultraviolet and visible (UV-vis) range is characteristic of electronic transitions [1]. Knowing which frequencies get absorbed the most by the sample provides information about the structure and function of the molecule or complex. Energies of vibrational modes directly inform about the Three-Dimensional (3D) molecular structure, such as the secondary structure of proteins [2]. Absorption peaks in the UV-vis frequency range elucidate the chemical structure, as specific atomic bonds correspond to specific frequencies, although influenced by their neighboring atoms [3]. However, the more complex the molecules get, the more overlapping and averaged the peaks will be, introducing great difficulty to interpreting the measured spectra [4]. Hence, multi-dimensional spectroscopy was introduced to resolve the overlapping peaks. The rest of this work focuses on Two-Dimensional Electronic Spectroscopy (2DES).

Using concepts from multi-dimensional Nuclear Magnetic Resonance (NMR) first suggested in 1971 and established in 1976 [5], the first 2DES experiment was realized using dye molecules in 2001 [6].

In linear absorption spectroscopy, the intensity of light at different frequencies is compared before and after passing through a sample. In 2DES, correlations between two frequency responses are studied [7]. A sequence of three ultra-fast, broadband laser pulses is sent into the sample. Varying the time between the first two pulses allows selecting a frequency that will constructively interfere to excite electronic states. The third pulse (probe) interacts with this state and creates a signal consisting of multiple frequency components. This way, a correlation between the excitation and probe frequencies can be measured and plotted in a 2D map after scanning over a range of excitation frequencies. Varying the time between the second excitation pulse and the probe pulse gives the system time to evolve or relax, resulting in time-evolving 2D spectra. Those spectra contain information about how electronic excited states were transferred or lost as time passed. This method has limitations, however. The concentration of sample molecules needs to be high [8], which is sometimes not possible due to preparation difficulty or aggregation.

A method that fixes this is Fluorescence-detected 2DES (F-2DES). Here, a sequence of four pulses is used instead of three, resulting in an excited state population [9] instead of coherent polarization oscillation. The requirement for high concentration is resolved by this, potentially enabling even single-molecule measurements [10]. Furthermore, background signal from scattering and the probe pulse, present in 2DES, can be avoided here by spatial separation [11]. This is because once the population of excited electrons is established, they spontaneously decay isotropically, enabling placement of a detector away from the pulse beam line(s). An application to microscopy is also possible, spatially detecting variations in fluorescence in a sample [12].

A price for all these advantages is a new artifact in the two-dimensional (2D) spectra. Cross-peaks (correlations between different frequencies) in the 2D spectrum are obscured

by an intense Exciton-Exciton Annihilation (EEA) background signal [13]. This was absent in standard 2DES because a coherent polarization was induced with three laser pulses, compared to F-2DES having four pulses populate two excited states that can annihilate before the incoherent fluorescence is emitted.

A proposed solution to this issue is time-resolving the fluorescent signal [14, 13]. Standard F-2DES integrates the total fluorescent signal since the last probe pulse until long enough for all excitons (electron-hole pairs resulting from electron excitations) to have decayed. It was instead suggested to use established methods for time-resolving the fluorescent signal [15].

This method is of interest especially in pigments and photosystems, where frequency-dependent excitation dynamics are the primary functions of the system. A well-studied exemplary system, Light Harvesting complex 2 (LH2) of purple bacteria (*Rhodoblastus acidophilus*) is used in this thesis. We computationally model the new time-resolved F-2DES and interpret the information contained in the 2D spectral evolution.

2 Theory & Simulation Methods

In Section 1, Two-Dimensional Electronic Spectroscopy (2DES) and its Fluorescence-detected variant (F-2DES) were introduced and motivated. This section explains the principles in more detail to clarify the improvements enabled by the novel time-resolved method. This is necessary to understand the results and their analysis in Section 3. First, 2DES is explained conceptually, after which the differences with F-2DES are better clarified. The fluorescence detection method is introduced more quantitatively and procedurally in the context of simulation. Lastly, the time-resolved response is defined. The theory follows Ref. [7] for 2DES and Ref. [16] for F-2DES, as well as the theory and methods section from Ref. [13].

2.1 2D Electronic Spectroscopy (2DES) overview

In standard 2DES, a sequence of three ultra-fast laser pulses is used with time delays between them t_1 and t_2, and a time t_3 between the last pulse hitting the sample and the signal being measured [1, 6, 7]. The narrow pulses in the time domain will be correspondingly wide in the frequency domain, as seen from the Fourier theorem. The first pulse induces oscillations in the sample at the charges' respective natural frequencies. Depending on t_1, the states will accumulate different phases only to interact with the second pulse either constructively or destructively. After a mixing period t_2, the third pulse hits the sample, and the signal is measured afterwards as a function of t_3. From this, a background linear signal from just pulse 3 is subtracted to isolate the non-linear effects due to excitation dynamics. Using a Fourier Transform (FT) on t_3, a frequency spectrum of ω_3 is obtained for those values of t_1,t_2, quantifying at which frequencies the detected signal oscillated and how much. By repeating the experiment for a range of t_1 values, the interference of the first two pulses will vary due to different frequency contributions, which can again be quantified using FT on t_1 to get signal dependence on ω_1. A 2D plot of the non-linear signal intensity as a function of ω_1, ω_3 is obtained, representing the correlation between the excitation and detection frequencies and so capturing the coupling of the electronic states. In the waiting time t_2 between excitation and probe pulses, the initial excited states have time to decay or transfer to different states. Repeating the procedure for multiple t_2 reveals the dynamics of the electronic states.

2.2 Fluorescence detected 2DES (F-2DES)

F-2DES works similarly to standard 2DES, but it uses 4 laser pulses, with the time delays between them t_1, t_2, t_3 and a time t_4 after the fourth pulse [9, 17]. The signal measured is not a coherent polarization as in the 2DES case, but instead an incoherent fluorescence, meaning spontaneous emission of photons in any direction. The 4 pulses can interact in eight distinct ways, shown in Fig. 1, resulting in a singly or doubly excited state. Those states then decay radiatively (photon emission through fluorescence) or non-radiatively (heat). The expected number of photons emitted by a single excited state is denoted as quantum yield $0 \leq Q^{(1)} \leq 1$, while the doubly excited state defines $0 \leq Q^{(2)} \leq 2$.

Ground state bleach (GB) corresponds to the first pulse exciting some ground states, leading to less subsequent absorption at this frequency, resulting in a negative signal by convention. Stimulated emission (SE) means that after the first pulse excites a state, a second pulse at the right frequency can stimulate emission of this state, resulting in two emitted photons. This means more photons at this frequency passed through, and so fewer of them were absorbed, also resulting in a negative signal. Excited state absorption (EA) enables absorption at new frequencies now accessible from the first excited state, resulting

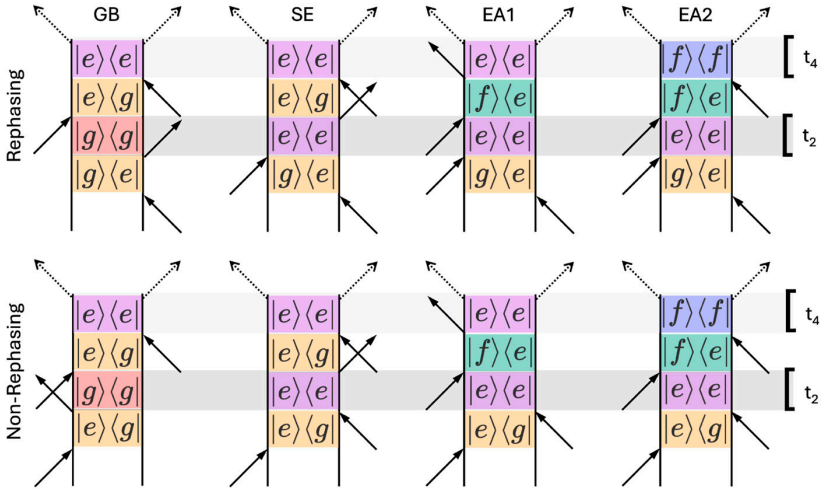

Figure 1: The Feynmann diagrams of a 4 pulse F-2DES. Time flows from bottom up, 4 solid pulses affect the quantum bra or ket state (right/ left) and point towards or away from the diagram (constructive/ destructive effect). Dotted pulses represent incoherent fluorescent decay. g,e, and f stand for ground, excited, and doubly excited states, respectively. Mixed letter rows correspond to coherent superpositions. Non/rephasing pathways differ by whether the phase was switched between t_1 and t_3. Figure obtained from [13] with permission.

in higher absorption at those frequencies and so a positive signal. EA1 and EA2 differ in the effect of the 4th pulse, resulting in singly and doubly excited populations, respectively.

2.3 Non-linear response

The previous subsection hinted that the quantity of interest is not the raw fluorescence (photon count), but a difference from a linear signal. This is done because the majority of the raw fluorescence comes from just the excitons created by the first two pulses, or those just from the last two. But the interaction between the two excitons causes a deviation from these independent signals. And it is these interactions that shine light (pun intended) on the energy transfer dynamics in the molecular systems of interest. By seeing how this non-linear signal changes with t_2, the movements of the excitons can be discerned as from frames of a movie.

Since the fluorescent photons are spontaneously emitted in all directions, this is achieved experimentally by repeating the experiment with multiple combinations of phase shifts of the 4 laser pulses [17]. The linear signal from the first two pulses will not depend on the phases of pulses 3 and 4, and vice versa. On the other hand, the non-linear response will change with every phase change. By correctly combining the signals from different phase combinations, the linear component cancels out despite contributing the majority of the raw signal.

2.4 Coarse-Grained exciton model of LH2

When modeling (F-)2DES, it is computationally necessary to avoid simulating every atom explicitly. Hence, the system is divided into segments that interact weakly with each other compared to interactions of sites within a segment, using the protocol from Ref. [13]. Then the excitation energy transfer between segments is on a much longer scale, such that excitations within segments have reached equilibrium states [18]. This allows for the treatment

of this incoherent exciton transfer between segments using a population transfer matrix P_{ji} during the time between the two pulse pairs:

$$p_j(t_2) = \sum_i P_{ji}(t_2) p_i(0) \tag{1}$$

where $p_j(t_2)$ is a population vector representing the proportion of states on segment S_j.

All molecular sites are modeled as two-level systems, with a ground state and an optically accessible excited state. The Frenkel exciton Hamiltonian for sites within a segment S_i is [19]:

$$H^i(t) = \sum_{n \in S_i} \epsilon(t) B_n^\dagger B_n + \sum_{n,m \in S_i} J_{nm}(t) B_n^\dagger B_m \tag{2}$$

with creation and annihilation operators $B^\dagger, B$. Terms $\epsilon(t)$ and $J_{nm}(t)$ are the excitation energy of molecule n and the coupling between molecules n, m within segment S_i. They are time-dependent to reflect fluctuations in the environment, causing broadening of the spectral peaks (a range of energies corresponding to a transition). The fluctuations are simulated by an overdamped Brownian oscillator.

The Hamiltonian corresponding to couplings between segments is:

$$H^{ij} = \sum_{n \in S_i, m \in S_j} J_{nm} B_n^\dagger B_m \tag{3}$$

with segments S_i, S_j, creation and annihilation operators $B^\dagger, B$, and coupling J_{nm} between molecules n, m in segments S_i, S_j, assumed to be independent of local fluctuations. The full Hamiltonian is the sum of all individual segment Hamiltonians and the inter-segment interaction Hamiltonians.

Here, the Multichromophoric Förster Resonance Energy Transfer (MC-FRET) method [20] is used to obtain a Rate matrix K from the two Hamiltonians, averaging over a large number of random fluctuation trajectories. The rate matrix then directly translates to a population transfer matrix describing the incoherent energy transfer between segments:

$$P_{ji}(t) = [\exp(t_2 K)]_{ji} \tag{4}$$

The structure of LH2 of *Rhodoblastus acidophilus* shown in Fig. 2 motivates using a separate segment for each of the nine B800 chromophores due to their spacing. On the other hand, the B850 chromophores are tightly packed, meaning the incoherent energy transfer assumption would be inaccurate. This is why the eighteen B850 chromophores will constitute the 10th segment.

2.5 Response function

Assuming the transfer between the 10 defined segments only happens during waiting time t_2, the response of the sample to the 4 pulses can be split into 3 distinct parts: excitation, waiting time, and signal emission. This splitting follows the Doorway-Window formalism [22]. The response function represents the nonlinear fluorescent signal as a function of t_1, t_2, t_3:

$$\begin{aligned} R^{||}(t_1, t_2, t_3) = \sum_{i,j}^{N_S} \left[D_i^R(t_1) + D_i^{NR}(t_1) \right] P_{ji}(t_2) \Bigg[\sum_d^{GB,SE,EA} Q_j^{(1)} W_j^d(t_3) + \\ Q_{jj}^{(2)} W_j^{EA} + \sum_{k \neq j} \left(2Q_j^{(1)} - Q_{jk}^{(2)} \right) W_k^{GB}(t_3) \Bigg] \end{aligned} \tag{5}$$

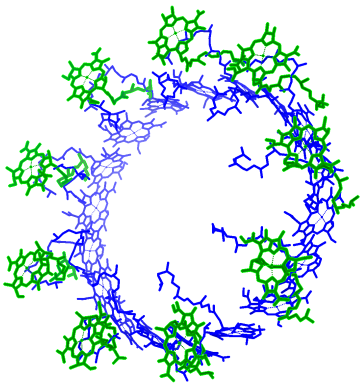

Figure 2: LH2 structure with protein scaffold removed. Nine green spaced out B800 chromophores and eighteen blue stacked B850 chromophores. Figure generated in ChimeraX [21].

up to weighting by molecule orientation with respect to the pulse propagation axis $A^{||}_{\alpha\beta\gamma\delta}$ [23] with different $W^{d}_{j,\gamma\delta}$ and $D_{i,\alpha\beta}$ for each case. The structure of Eq. (5) is indicative; D_i represents the Doorway function (a sum of Rephasing and Non-rephasing components), capturing the exciton population of segment i as a response to the first two laser pulses separated by t_1. Next, $P_{ji}(t_2)$ evolves this population during the waiting time t_2 as seen in Eq. (1). Finally, the fluorescence response to the evolved population is given by the Window functions, specific to each of the 4 pathways given in Fig. 1. The Window functions are scaled by the quantum yields, as only a fraction of excitations releases photons when de-excited. The first term in the Window part represents GB, SE, and EA1 pathways, scaled by Q_1 because one exciton is left in the segment after the fourth pulse. The second term describes EA2, scaled by Q_2 as two excitations remain on the same segment. The last term also corresponds to EA2, but for the cases where the two excitons are on different segments. The $||$ superscript indicates that the 4 laser pulses were polarized parallel to each other, which is the focus of this work. Analogous response functions can be obtained for other polarization combinations using the proper weighting factors A. Explicitly, the Doorway and window functions are obtained by Numerical integration of the Schrödinger equation (NISE) using a C package available on GitHub [18, 24]. They consist of subsequent application of time evolution operators and transition-dipole operators that (de)excite the state, as captured in Fig. 1. The expressions can be found in the appendix of Ref. [13].

When the response function is Fourier Transformed twice (along t_1 and t_3), a 2D spectrum is obtained: $S^{||}(\omega_1, t_2, \omega_3)$, the change in fluorescence intensity as a function of the two pulse frequencies, for a particular waiting time t_2.

2.6 Quantum yield time evolution

While the Doorway and Window functions in Eq. (5) can be calculated from transition-dipole operators and time evolution matrices, and the population transfer matrix is calculated from the rate matrix obtained from MC-FRET, the last missing pieces are the quantum yield factors. Previously [13], the factors were only calculated for long detection time $t_4 \to \infty$ after the last laser pulse. The excitations would completely decay, and the proportion of this total decay being radiative was denoted Q. Experimentally, this corresponds to counting the emitted photons after the fourth pulse without time resolution.

In this work, we for the first time make the quantum yield factors time-dependent. Then, quantum yields represent the expected number of photons emitted in the time t_4 after the last laser pulse. While this has not been experimentally realized at the time of writing, either counting all photons until a given t_4 or noting the arrival time for each one and integrating the signal up to t_4 are the experimental equivalents. The code used can be found at https://github.com/EdWin939/Time_Resolved_F-2DES.

First, let us define all possible exciton states taking the formalism from Ref. [13]. The system starts with two excitons on segments S_i, S_j ($i = j$ is possible). Let us label this state ij. The order does not matter, so the smaller number shall be first. If one exciton moves from S_j to S_k, the new state is ik. This movement is governed by the Rate matrix K found from MC-FRET. If the exciton in S_k then decays radiatively (emitting a photon), the new state is labeled iR, whereas a non-radiative decay (heat) would result in the iN state. The order is not important, so if the S_i was the one to radiate, kR would be left. In either case, there is now only one exciton left in the system. It can still be transferred to different segments under K, but can never regain a second excitation. Eventually, the second exciton will also be lost, resulting in one of the 3 final states: RR, NR, NN.

This state evolution behavior can be described by a Quantum yield rate matrix K^Q:

$$\frac{ds_a(t)}{dt} = \sum_b K^Q_{ab} s_b(t) \tag{6}$$

where $\vec{s}$ is the state vector. For an N-segment system, its length is $\frac{N(N+1)}{2} + 2N + 3$, where the terms represent the two excitons, the one exciton left after (non)radiative decay, and the three decayed states, respectively. An example matrix for $N = 4$ is shown in Fig. 3.

The solution to Eq. (6) is:

$$\vec{s}(t_4) = \exp\left(t_4 K^Q\right) \vec{s}(0)$$

where $\vec{s}(0)$ is the initial state lets us write:

$$Q^{(2)}_{jk}(t_4) = 2s_{RR}(t_4) + s_{NR}(t_4); \quad s_a(0) = \delta_{a,jk} \tag{7}$$

$$Q^{(1)}_{j}(t_4) = s_{NR}(t_4); \quad s_a(0) = \delta_{a,Nj} \tag{8}$$

with δ the Kronecker delta. Equations 7 and 8 are intuitive, representing the proportion of excitons initially on a segment (pair) that decay radiatively within detection time t_4. For double excitations, s_{RR} is counted twice as RR represents two photons emitted, while NN contributes no photons. Since the diagonal of K^Q is constructed to conserve the magnitude of $\vec{s}$, sensibly $0 \leq Q^{(2)}(t_4) \leq 2$ and $0 \leq Q^{(1)}(t_4) \leq 1$ as mentioned earlier.

With time-dependent quantum yields, we can generalize Eq. (5):

$$\begin{aligned} R^{||}(t_1, t_2, t_3, t_4) = \sum_{i,j}^{N_S} \left[D_i(t_1)\right] P_{ji}(t_2) \Bigg[\sum_{d}^{GB,SE,EA} W^d_j(t_3) Q^{(1)}_j(t_4) + \\ W^{EA}_j(t_3) Q^{(2)}_{jj}(t_4) + \sum_{k \neq j} W^{GB}_k(t_3) \left(2Q^{(1)}_j(t_4) - Q^{(2)}_{jk}(t_4)\right) \Bigg] \end{aligned} \tag{9}$$

	11	12	13	14	22	23	24	33	34	44	1N	2N	3N	4N	1R	2R	3R	4R	NN	NR	RR
11		k_{21}	k_{31}	k_{41}	0	0	0	0	0	0	0	0	0	0	0	0	0	0	0	0	0
12	$2k_{12}$		k_{32}	k_{42}	$2k_{21}$	k_{31}	k_{41}	0	0	0	0	0	0	0	0	0	0	0	0	0	0
13	$2k_{13}$	k_{23}		k_{43}	0	k_{21}	0	$2k_{31}$	k_{41}	0	0	0	0	0	0	0	0	0	0	0	0
14	$2k_{14}$	k_{24}	k_{34}		0	0	k_{21}	0	k_{31}	$2k_{41}$	0	0	0	0	0	0	0	0	0	0	0
22	0	k_{12}	0	0		k_{32}	k_{42}	0	0	0	0	0	0	0	0	0	0	0	0	0	0
23	0	k_{13}	k_{12}	0	$2k_{23}$		k_{43}	$2k_{32}$	k_{42}	0	0	0	0	0	0	0	0	0	0	0	0
24	0	k_{14}	0	k_{12}	$2k_{24}$	k_{34}		0	k_{32}	$2k_{42}$	0	0	0	0	0	0	0	0	0	0	0
33	0	0	k_{13}	0	0	k_{23}	0		k_{43}	0	0	0	0	0	0	0	0	0	0	0	0
34	0	0	k_{14}	k_{13}	0	k_{24}	k_{23}	$2k_{34}$		$2k_{43}$	0	0	0	0	0	0	0	0	0	0	0
44	0	0	0	k_{14}	0	0	k_{24}	0	k_{34}		0	0	0	0	0	0	0	0	0	0	0
1N	$k_1^{A1}+2k_1^N$	k_2^N	k_3^N	k_4^N	0	0	0	0	0	0		k_{21}	k_{31}	k_{41}	0	0	0	0	0	0	0
2N	0	k_1^N	0	0	$k_2^{A1}+2k_2^N$	k_3^N	k_4^N	0	0	0	k_{12}		k_{32}	k_{42}	0	0	0	0	0	0	0
3N	0	0	k_1^N	0	0	k_2^N	0	$k_3^{A1}+2k_3^N$	k_4^N	0	k_{13}	k_{23}		k_{43}	0	0	0	0	0	0	0
4N	0	0	0	k_1^N	0	0	k_2^N	0	k_3^N	$k_4^{A1}+2k_4^N$	k_{14}	k_{24}	k_{34}		0	0	0	0	0	0	0
1R	$2k_1^R$	k_2^R	k_3^R	k_4^R	0	0	0	0	0	0	0	0	0	0		k_{21}	k_{31}	k_{41}	0	0	0
2R	0	k_1^R	0	0	$2k_2^R$	k_3^R	k_4^R	0	0	0	0	0	0	0	k_{12}		k_{32}	k_{42}	0	0	0
3R	0	0	k_1^R	0	0	k_2^R	0	$2k_3^R$	k_4^R	0	0	0	0	0	k_{13}	k_{23}		k_{43}	0	0	0
4R	0	0	0	k_1^R	0	0	k_2^R	0	k_3^R	$2k_4^R$	0	0	0	0	k_{14}	k_{24}	k_{34}		0	0	0
NN	k_1^{A0}	0	0	0	k_2^{A0}	0	0	k_3^{A0}	0	k_4^{A0}	k_1^N	k_2^N	k_3^N	k_4^N	0	0	0	0		0	0
NR	0	0	0	0	0	0	0	0	0	0	k_1^R	k_2^R	k_3^R	k_4^R	k_1^N	k_2^N	k_3^N	k_4^N	0		0
RR	0	0	0	0	0	0	0	0	0	0	0	0	0	0	k_1^R	k_2^R	k_3^R	k_4^R	0	0	

Figure 3: The K^Q for a four-segment system. The matrix is not symmetric, because states can only decrease their number of excitons with time. The red sub-matrices are identical Ks from Eq. (4) and come from MC-FRET, describing hopping of an exciton between segments. The yellow matrix represents the same for two excitons, with only one transition allowed at a time (hence the 0s), and some rates doubled. This is because state 33 has the rate of changing to 31 double that of individual 3 changing to 1, as either exciton can hop. The green and pink row sub-matrices represent non-radiative and radiative decays of a single exciton with (possibly segment-specific) externally defined rates. The dark-green and purple block sub-matrices use combinations of the same decay entries, this time from doubly to singly excited states, again with doubled or 0 rates as in the yellow sub-matrix. Importantly, the dark-green one also includes Annihilation rates, where two excitons on the same segment annihilate into one non-radiatively. The beige row sub-matrix represents annihilations of two excitons into zero. These rates are set to 0 for this study, enabling labeling of annihilation into a single exciton as k_i^A. The diagonal elements are left out for clarity, and ensure the sum of each column is 0 to conserve the total population. Figure borrowed from [13] with permission.

again up to weighted addition with the same coefficients and variable D, W as mentioned after Eq. (5). Eq. (9) gives the final (parallel-polarized) spectrum $S^{||}(\omega_1, t_2, \omega_3, t_4)$ after double Fourier Transform.

Importantly, constructing the K^Q requires both the Rate matrix K from MC-FRET, and specifying three timescale parameters, inverses of the rates mentioned in the caption of Fig. 3 as K^Q entries. The first is the fluorescent lifetime τ^F, describing how quickly an exciton decays overall. The second is that the radiative lifetime τ^R is the timescale of an exciton emitting a photon. The Non-Radiative losses are then already given by $\frac{1}{\tau^{NR}} = \frac{1}{\tau^F} - \frac{1}{\tau^R}$. The last is the EEA timescale τ^A, a lifetime of two excitons on the same segment annihilating into one. While all of those could be segment-specific, this work only distinguishes EEA timescales for the two different segment types: $\tau^A_{B800}, \tau^A_{B850}$. Annihilations of two excitons into zero are not considered here. The default values are sourced from literature[14, 25, 26] as $\tau^A_{B800} = \tau^A_{B850} = 0.6$ p s, $\tau^F = 986$ ps,$\tau^R = 10$ ns.

As for the explicit t_4 evolution of Q factors, semi-quantitative predictions are possible. Namely, based on equations 7 and 8, $Q_1(0) = Q_2(0) = 0$, as none of the excited states could have instantly radiated, and any radiation during t_2 would be subtracted as a linear signal. Since single excitons decay either radiatively or non-radiatively with rates $k_R = \frac{1}{\tau^R}, k_{NR} = \frac{1}{\tau^{NR}}$, the probability of this exciton decaying radiatively is $Q_1(\infty) = \frac{k_R}{k_R + k_{NR}} = \frac{\tau^F}{\tau^R}$, for the default parameters $Q_1(\infty) \approx \frac{986ps}{10ns} \approx 9.86 \times 10^{-2}$. The double exciton quantum yield is more complicated due to EEA (which is ultimately the reason we can extract energy transfer information from Eq. (9)). Without EEA, Q_2 would just be double that of $Q(1)$, as two excitons decay independently of each other. But the real probability of excitons hopping to the same segment and annihilating non-radiatively to one means Q_2 will be less than double Q_1, while still remaining higher, because not all double exciton states will result in annihilation to a single exciton state.

3 Results & Discussion

The previous section explained the theory and procedure behind a time-resolved F-2DES measurement. Next, we show what new information can be obtained from this simulation compared to standard F-2DES. First, F-2DES with fluorescence detection until $t_4 \to \infty$ is compared to a finite t_4 for a study of t_2 exciton dynamics. Next, for a fixed t_2, the evolution of the fluorescent signal during t_4 is examined. Subsequently, this evolution is compared between cases with different input annihilation rate parameters. Finally, for fixed parameters and t_2, the effects of the rate matrix K on the fluorescence throughout t_4 are shown.

3.1 F-2DES with finite t_4

First, we recreate the current F-2DES method by setting an infinite t_4 limit, with 10^{12} ps. This is sufficiently large for most decays to have taken place and for quantum yields Q_1, Q_2 to have stabilized to their asymptote values of 9.86×10^{-2} and 9.89×10^{-2}, respectively, with only minimal variation between segments. Fig. 4a shows a 2D spectrum obtained with this method at $t_2 = 0$. Two characteristic frequencies are present, as expected from two types of chromophores in LH2: B800 means $\lambda \approx 800nm$, corresponding to $\omega \approx 12500cm^{-1}$, and B850 has $\omega \approx 11600cm^{-1}$. Unlike in standard 2DES, cross peaks are present despite the zero waiting time, obscuring transfer dynamics. As mentioned in Section 1, this is attributed to Exciton-Exciton Annihilations (EEA) during the extremely long t_4. To quantitatively analyze these dynamics, four Regions of Interest (ROIs) were chosen, centered around the peaks. The amplitude within them is integrated in all subsequent peak evolution plots. Namely, Fig. 4b shows the evolution of the four peaks' integrated amplitudes as t_2 is varied in repeated runs and more excitons have had enough time to hop between segments or decay[1].

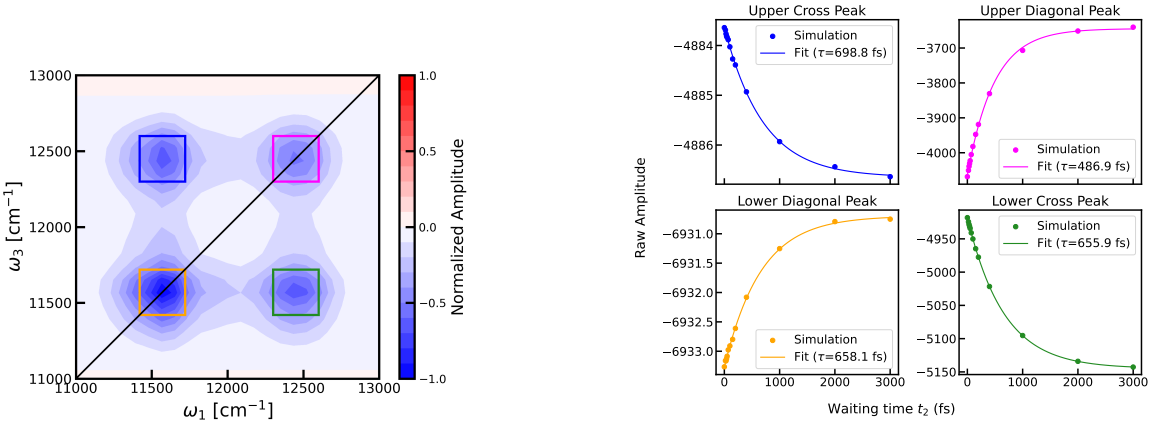

(a) 2D Spectrum at $t_2 = 0$ fs, $t_4 \to \infty$ (10^{12}ps)

(b) t_2 peak evolution ($t_4 \to \infty$)

Figure 4: Standard F-2DES. Fig. 4a shows a 2D spectrum, normalized by the highest peak while preserving sign. Regions of interest are highlighted. Fig. 4b shows the time evolution of the integrated amplitudes as t_2 is varied. Exponential fits are plotted, with cross-peaks growing towards an asymptote (into the negatives) and diagonal peaks decaying asymptotically (becoming less negative).

While Fig. 4b shows a nice exponential asymptotic behavior, the scale can be misleading. Despite having similar decay timescales, the relative decay over the same t_2 range is drastically different between them. In an experimental setting with noise and uncertainties, the

[1]Note that Ref. [13] found a timescale of around 500 ps for the upper cross peak. The methodologies are to be compared, but this has no impact on the rest of the results.

relative decay scale is desired to be maximized. Fig. 5a shows the normalized signals on an absolute scale from 0, highlighting the low contrast. In this case, uncertainties may hide the nice exponentials. Fig. 5b shows the same experiment, but with fluorescence only measured until a finite time $t_4 = 0.1$ ps, providing much better contrast except in the lower diagonal ROI. Notably, $t_4 = 10$ ps produces indistinguishable contrast from $t_4 = \infty$, suggesting decreasing t_4 to the order of EEA timescales (here 0.6 ps) may be necessary to improve the signal.

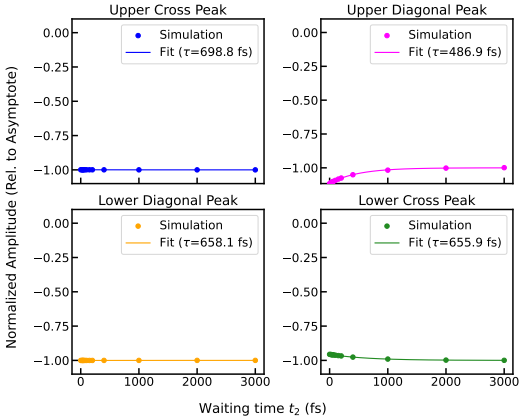

(a) Peak evolution in t_2 normalized by the fitted asymptote (preserving sign), $t_4 \approx \infty$

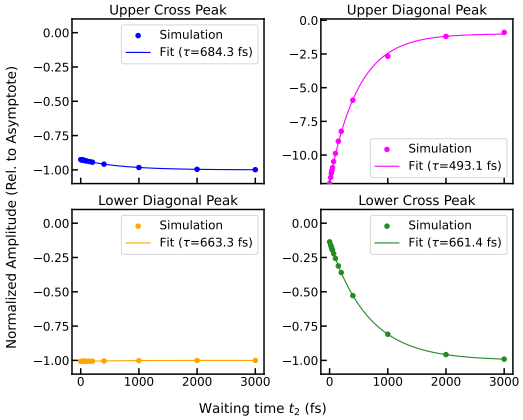

(b) Peak evolution in t_2 normalized by the fitted asymptote (preserving sign), $t_4 = 0.1$ ps

Figure 5: Normalized evolution of the four peaks throughout t_2 for 5a standard infinite t_4 (same as Fig. 4b), 5b proposed finite t_4. Each subplot was normalized by the asymptote value while preserving sign. Graphs are shown from 0 to highlight relative growth differences. The transition is gradual, enabling a search for the best experimental t_4 with a strong enough contrast but not too weak overall signal.

A price for decreasing measurement time t_4 to improve the signal-to-noise ratio is a lower absolute signal. As seen in Eq. (9), the signal is scaled by the Q factors. Fig. 6a shows how quantum yields vary with t_4 over multiple magnitudes. A trade-off between signal and noise ratio needs to be optimized in experiments to give the ideal t_4 value.

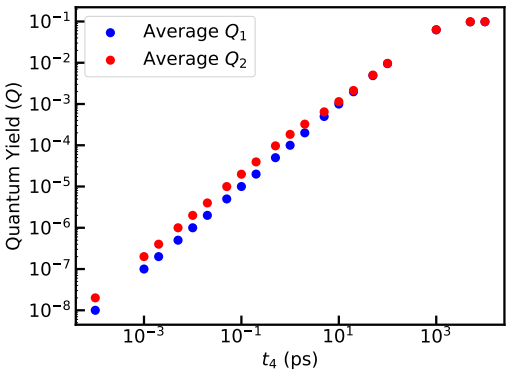

(a) Average quantum yields versus t_4

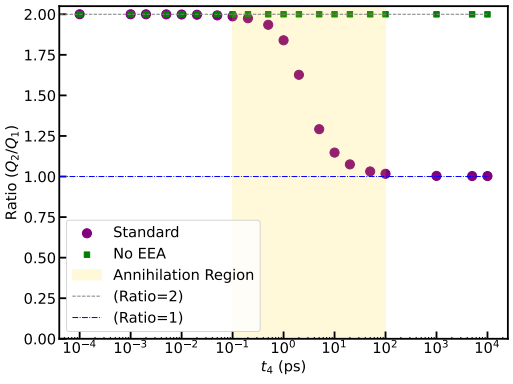

(b) $\frac{Q^{(2)}}{Q^{(1)}}$ with(out) EEA

Figure 6: Quantum yields' dependence on measurement time t_4. 6a shows the absolute Q factors, confirming that their magnitude decreases dramatically with decreased t_4. Not shown due to logarithmic scale, both $Q(0) = 0$. Furthermore, the factors plateau at a similar value of 0.099 already after 10000 ps. In 6b, the Q factor ratio is plotted, showing that its dynamics contain information about EEA.

Fig. 6b shows the ratio $\frac{Q^{(2)}}{Q^{(1)}}$ and that it is EEA that diverts it from 2 (2 independent excitons decaying with $Q^{(1)}$s). The asymptote at 1 for large t_4s indicates that, eventually, most exciton pairs undergo annihilation and the situation reduces to a single exciton $Q^{(1)}$. This motivates studying the t_4 dependence of the signal for a fixed t_2, discussed next.

3.2 Time (t_4) evolution of the Fluorescence-detected 2D spectrum

As shown in Fig. 6b, the quantum yield ratio changes during t_4 due to EEA. Furthermore, EEA is only modeled to happen with two excitons in a single segment, due to the large spatial separation of the segments. Those two facts indicate that studying the t_4 evolution of the spectra for a fixed t_2 (here t_2=0) contains information about exciton transfer dynamics. This is because if the excitons are transferred to occupy the same segment, EEA can occur and change the quantum yields non-trivially (outside the average signal growth due to more and more fluorescent decays). Note the difference compared to fixed t_4 and varying t_2 in Fig. 4, where the first exciton hopped during t_2 without a chance to annihilate. After the second exciton was created, only the accumulated effect of their hopping and possible EEA was captured in the total signal until t_4.

Fig. 7a shows the integrated peak signal as a function of t_4 for fixed $t_2 = 0$ fs. Here, the signal grows from zero to an asymptote (limited total emitted photons) at a consistent timescale ≈ 987 ps, which is almost exactly the fluorescent timescale $\tau^F = 986$ ps [26] inputted into the K^Q matrix. As mentioned above, this is the trivial growth (more and more photons getting emitted), hiding the energy transfer dynamics. To escape this without requiring prior knowledge of the τ^F (as would be the experimental case), all signals are normalized by the Upper Diagonal (UD) peak values in Fig. 7b and from now on. The choice was partly arbitrary between this and Lower Diagonal (LD), as cross-peaks are the main subjects of study of the energy transfer (correlations between different frequency states).

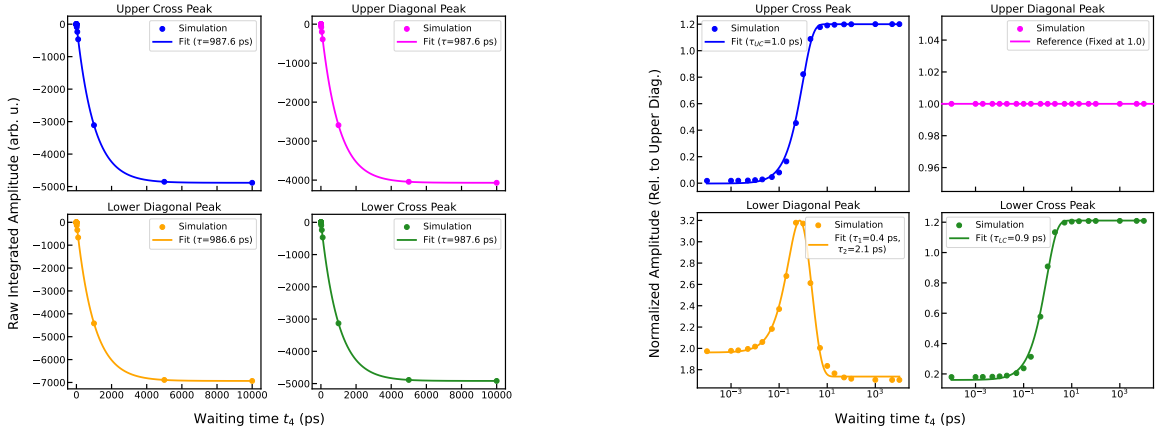

(a) Raw fluorescent peaks versus t_4

(b) Peaks normalized by upper diagonal

Figure 7: Evolution of the fluorescent signal during t_4. 7a has the raw signal while 7b has signal normalized by the Upper Diagonal values. The fits are exponential decays, except the normalized Lower Diagonal peak, which is bi-exponential (difference of two decaying exponentials. τ_1 is the timescale of the same sign as the single exponential fits). All normalized plots are positive due to being normalized by one of the originally all negative plots, meaning growth still represents a signal getting more negative.

Fig. 7b shows features originally obscured by the long τ^F in the raw data. The cross peaks grow relative to the UD at a timescale of ps, rather than hundreds of ps. The LD

gains a bi-exponential behavior after normalization. This represents the relative growth of the two diagonal peaks, and so the two timescales can likely be interpreted as each belonging to one diagonal peak. Since annihilation is more likely in the B850 than B850, it is then faster, and so the rising, faster timescale likely belongs to the LD proper, while the slower decaying timescale corresponds to UD growing and the normalization causing division by a slowly growing number. Note that the normalized peak evolution does not start at 0. This is because at $t_4 = 0$, both are zero, and their ratio is indeterminate, while at all subsequent times (shown on a logarithmic scale) the normalized quantity turns out not to be zero, as other peaks also appear, albeit in a small initial proportion to the UD.

To properly understand what the ROI evolution timescales say about annihilation and transfer rates in LH2, those internal rate parameters need to be varied and the ROI timescales compared between these parameter sets. This is done in the next subsection for EEA rates through $\tau^A_{B800}, \tau^A_{B850}$. The subsection after that analyses the ROI fit behavior for different population Rate matrices K.

3.3 Evolution dependence on empirical parameters

While it is clear that the plots in Fig. 7b contain information about the combination of exciton transfer and annihilation dynamics, the correspondence is not discernible as of yet. For this reason, we next observe how those plots change depending on the timescales used for rates in K^Q mentioned in Section 2.6. Because we normalize out the Fluorescent timescale $\tau^F = 986$ ps, which would otherwise only stretch or contract the t_4 axis, this parameter will be kept constant. Similarly, the radiative timescale will be fixed at $\tau^R = 10ns$, much larger than the rest, leading to very low rates.

It is the two EEA timescales, one for each segment type, that are the most directly involved in the signal and will be varied independently. The original model used the same value of $\tau^A_{B800} = \tau^A_{B850} = 0.59$ ps. Because of the exponential character and the large span of magnitudes of different processes' lifetimes, the annihilation timescales will be varied logarithmically one magnitude up and one down, with seven values between 0.06 ps and 6.0 ps. Furthermore, two extreme cases will be examined: 10^{-4} ps representing zero timescale (infinite annihilation rate), and 10^6 ps being infinite timescale (zero annihilation rate). Those finite values are chosen for numerical stability at two orders of magnitude below and above all the other timescales. This gives 81 parameter combinations, each producing a normalized set of plots like Fig. 7b. The best fit timescales of those plots are compared between the 81 parameter sets. As a reminder, everything is done for $t_2 = 0$ so that the full dynamics are captured in the t_4 signal.

3.3.1 Upper Cross-peak

Fig. 8 shows the analysis of the Upper Cross-peak ROI. Most notably, the EEA rate in B800 seems to have only a small influence on UC transfer time τ_{UC}, with only 10% change for the literature value of $\tau^A_{B850} = 0.6$ ps. The correlation is negative, so increasing τ^A_{B800} decreases the fitted τ_{UC}. The reason for this or the justification of the fit is not clear at this moment, as speeding up any annihilation process was expected to speed up the total signal. On the other hand, varying the EEA rate in B850 changes the UC transfer by orders of magnitude. This confirms that the signal comes predominantly from EEA in B850, meaning there is a great net flux of excitons from the outer B800 segments to the central B850,

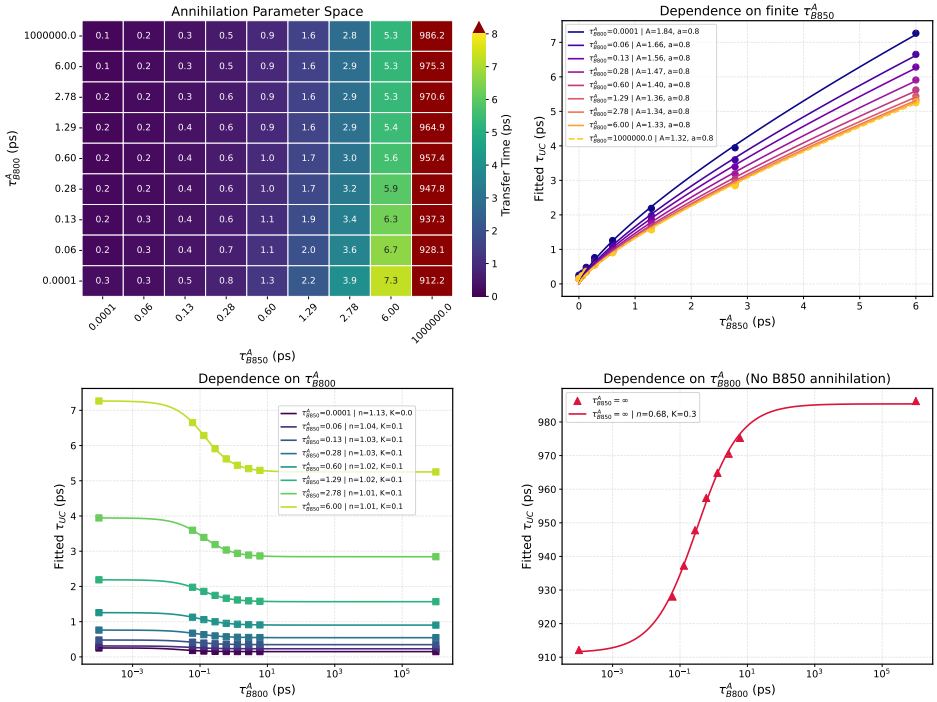

Figure 8: Upper Cross-peak growth timescale τ_{UC} for different annihilation lifetime combinations. Top left: heatmap of the 81 parameter sets. Top right: Dependence on τ^A_{B850} at fixed levels of τ^A_{B800} with power fit $\tau_{UC} = A(\tau^A_{B850})^a$. Bottom: Dependence on τ^A_{B800} at fixed levels of τ^A_{B850} with sigmoid fit $\tau_{UC} = C + \frac{A}{1+\left(\frac{\tau^A_{B800}}{K}\right)^n}$.

where they annihilate. This can be confirmed internally with the rate matrix K used for the simulation, which indicates that the rate from B800 to B850 was around $1.5\,\mathrm{ps}^{-1}$ with the opposite rate only $1.3\times10^{-3}\,\mathrm{ps}^{-1}$. The rate between two neighboring B800 sites was $1.8\,\mathrm{ps}^{-1}$.

While turning off B800 annihilation did not introduce any qualitative changes, turning off B850 annihilation resulted in a completely different regime with timescales a hundred times longer. Within a turned-off B850 annihilation, slowing down the B800 annihilation slows down the UC growth. This is likely because the annihilations on B800 that were usually overshadowed by B850 were now the only signal source. Once both annihilations were effectively turned off, a timescale 986 ps is recovered, identical to τ^F, hinting that the normalization by UD no longer reveals any new dynamics. Notably, the raw signal with turned off annihilations is far weaker than the default one (4 to 100 times depending on the peak), further solidifying EEA as the main signal source. This is shown in Fig. 9.

While there is no quantitative argument for the sigmoid fit in Fig. 8 of τ_{UC} dependence on τ^A_{B800} with turned off B850 annihilation, the physical reasoning is possible. When the B800 annihilation is sufficiently fast, the limiting factors are the transfer rates, with both excitons having to meet on the same B800 despite net flux towards B850. When the B800 annihilation is slow or nonexistent, the slowest timescale of the signal is the τ^F, hence the sigmoid between two asymptotes.

3.3.2 Lower Cross-peak

In a similar fashion to Fig. 8, LC analysis is shown in Fig. 10, showing mostly identical results. One important difference is the behavior with turned-off B850 EEA, where instead of

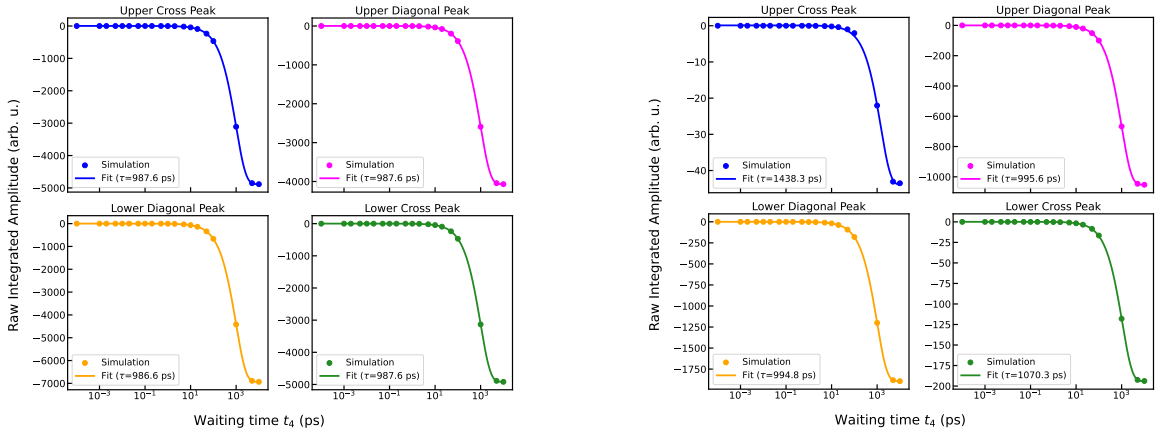

(a) Raw fluorescent peaks versus t_4

(b) Raw fluorescent peaks versus t_4, $\tau^A_{B850} = 0$

Figure 9: Comparison of absolute signal strengths for standard $\tau^A_{B800} = 0.6$ ps with a) standard EEA, b) no B850 EEA. Both subfigures show exponential decays on log x-axes, with a) the same as Fig. 7a.

a simple exponential, a bi-exponential fit is now necessary, as seen in Fig. 11 as an example. This additional complexity probably caused the sporadic behavior in the bottom right as compared to UC, due to bi-exponential fit instability. Apart from this case, the relationships between the fitted LC timescale τ_{LC} and either annihilation timescale are almost the same, including the parameters of the curves. This is not surprising, given the partial symmetry of the two cross peaks at $t_2 = 0$, as both represent the two excitons starting at different chromophore types, without either having had time to evolve before the second one was created (note the timescale of t_3 for this range of frequencies is $< 10^{-3}$ ps and $t_2 = 0$ fs). However, the situation is not completely symmetric. This is because when the first exciton is created in B850, it influences how a second exciton can be created there. The second exciton is harder to create due to the Pauli exclusion principle, so the peak will shift in the ω_3 axis. Then the LD peak evolves asymmetrically, eventually reaching into the UC but not the LC.

3.3.3 Lower Diagonal peak

As mentioned in Section 3.2, the rising and falling behaviour of the LD is interpreted as growth of LD divided by a (generally slower) growth of UD. Due to the fit instability and a narrower range of captured behaviours, the fit with a ratio of offset exponentials was avoided. Instead, a bi-exponential fit, meaning a sum (difference) of two exponential decays, was used. This is not a more drastic approximation compared to the ratio-of-exponentials fit, since the real dynamics is governed by a much more complicated combination of exponentials coming from the solution of Eq. (6).

Fig. 12 shows the two timescales for the same set of 81 parameters. The slices with one annihilation fixed are not shown due to their more complicated dependence than Figs. 8 and 10. Qualitatively, though, both the rise and fall dynamics get slower with slower B850 annihilation, solidifying B850 annihilation as the main mechanism behind UD growth, too. This is because even two excitons starting at two B800 segments are mainly influenced by τ^A_{B850}, not τ^A_{B800}, indicating that the majority of the UD signal comes from transfer of excitons to B850 and annihilation there. This could also explain the LD rise timescale being generally 10× shorter than the LD decay (UD growth) timescale.

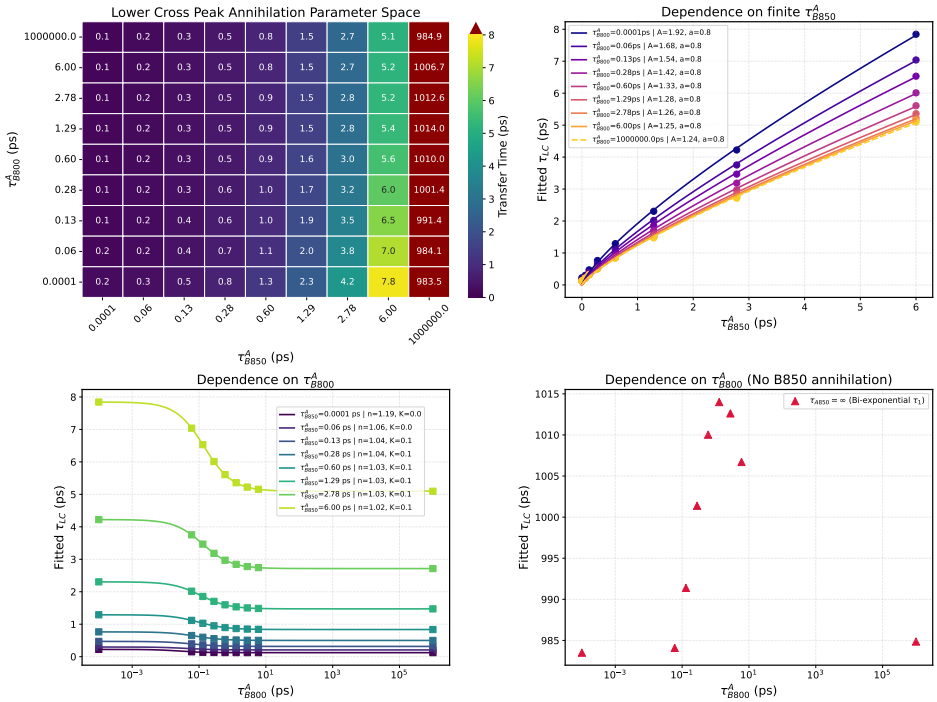

Figure 10: Lower Cross-peak growth timescale τ_{LC} for different annihilation lifetime combinations. Top left: heatmap of the 81 parameter sets. Note that the last column contains the corresponding peak growth timescale from a bi-exponential fit, not a simple exponential, as the rest of the heatmap. Top right: Dependence on τ^A_{B850} at fixed levels of τ^A_{B800} with power fit $\tau_{LC} = A(\tau^A_{B850})^a$. Bottom left: Dependence on τ^A_{B800} at fixed levels of τ^A_{B850} with sigmoid fit $\tau_{LC} = C + \frac{A}{1+\left(\frac{\tau^A_{B800}}{K}\right)^n}$. Bottom right: dependence of growth timescale from bi-exponential on τ^A_{B800} for zero B850 annihilation rate.

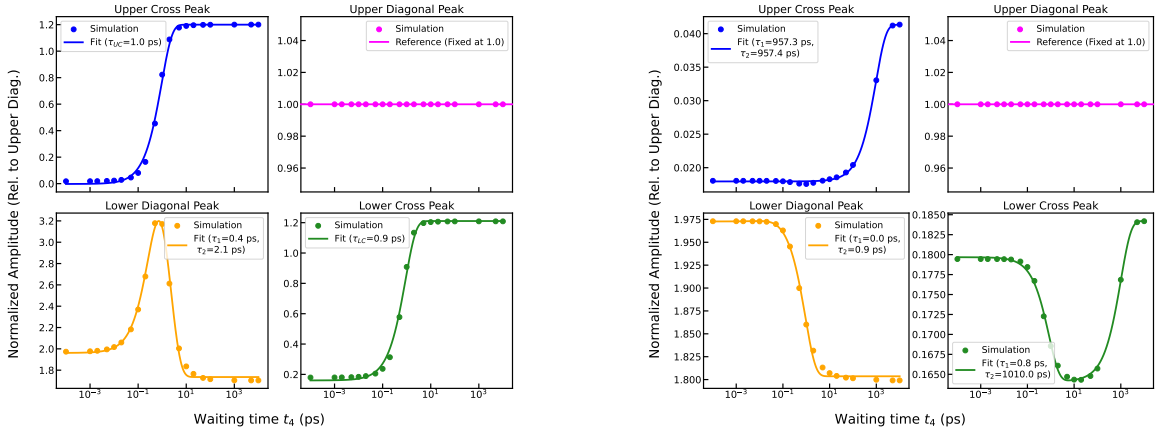

(a) Normalized peaks versus t_4

(b) Normalized peaks with no EEA

Figure 11: Four peaks' evolution in t_4. 11a has standard literature annihilation parameters. 11b has the same EEA timescale in B800 but no EEA in B850. Bi-exponentials are fitted in all regions but only contribute to the LC. Conversely, the usual bi-exponential LD behavior changes to simple exponential, although the normalized peak is getting smaller, not growing as usual. Curiously, the initial dip in the LC is also present in the UC but overshadowed by the subsequent growth.

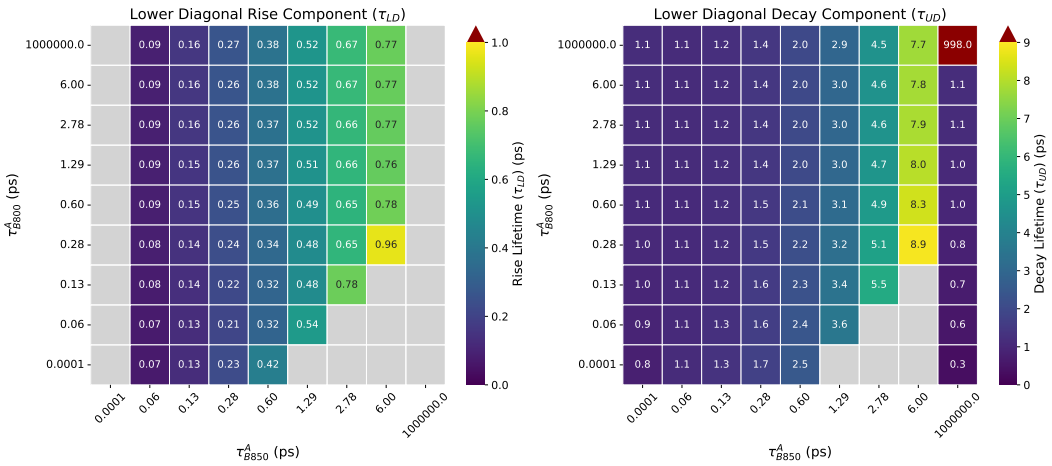

Figure 12: LD rise (left) and decay (right) timescales corresponding to LD rise and UD rise, respectively. Grey regions were left out due to negligible contribution (rightmost column), fit instability (leftmost column), and qualitatively different behaviour falling outside the bi-exponential model (bottom right region). Note that the regions bordering the bottom right also exhibit jumps compared to the regular regions around them.

This point gets even stronger once B850 annihilation is turned off. The rise component no longer influences the fit due to being negligible compared to the decay, as seen in Fig. 11b. This means that it is rare for two excitons starting at B850 to annihilate on B800, limiting the LD growth. While the majority of the LD decay (UD growth) signal disappears as the B850 pathway is turned off, the leftover signal annihilating on B800 is at a faster timescale corresponding to movement between B800 segments and annihilation there. Furthermore, faster B800 annihilation speeds up this process as expected, eventually bottlenecked by transfer between B800 segments.

At ultra-fast B850 annihilation, the LD growth becomes too fast and destabilizes the fit again, despite qualitatively aligning with the theory as shown in Fig. 13. In contrast, neither ultra-fast nor ultra-slow B800 annihilation changes the behaviour drastically, again due to the majority of the signal coming from B850 annihilation. Turning off both annihilations retrieves the $\tau^F = 986$ ps timescale, the same as in Figs. 8 and 10.

Lastly, the bottom right parameter space region was left out due to complicated behaviors that are no longer possible to be modeled by rise and fall. An example is shown in Fig. 14. The progressive switching of rise and fall could reveal information about transfer and B850 annihilation dynamics, but was not explored further in this study due to the more complicated behaviour in the in-between steps.

3.4 Evolution dependence on Rate matrix K

The previous subsection analyzed the variation of EEA timescales to gauge whether their effect is measurable in the t_4 signal. Here, we will analyze the variation of the Rate matrix K obtained from MC-FRET. While more general exploration is possible in the future, here we only scale the default matrix by a constant factor, preserving the relative transfer rate ratios. This will still vary the relative speed of transfer compared to annihilation.

Since we are studying $t_2 = 0$ fs case, K scaling will not play a role in Eq. (1), instead only influencing the transfer parts of K^Q as detailed in Fig. 3. This also means that the

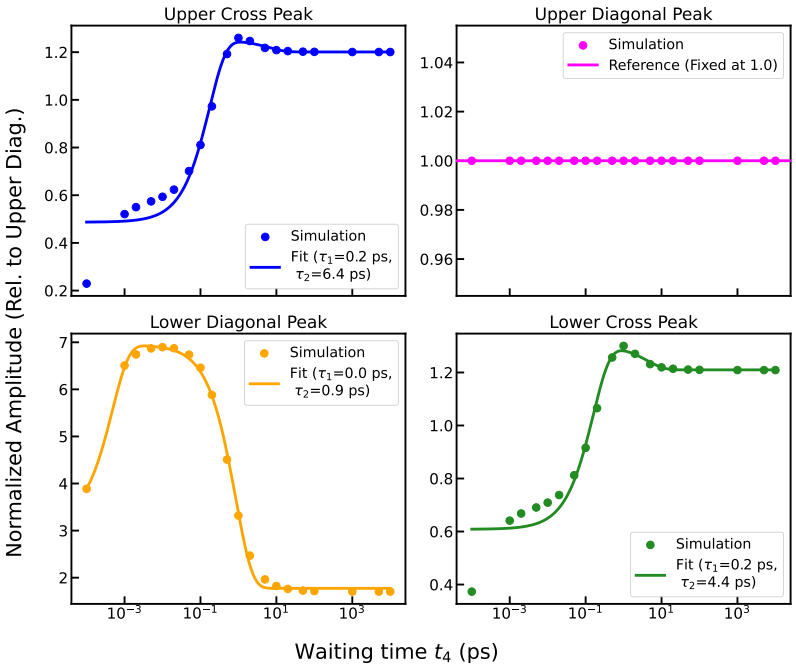

Figure 13: Extreme case of the peak evolutions with ultra-fast B850 annihilation and $\tau^A_{B800} = 0.2785$ ps. Only the decay timescale of LD and the growth timescales of cross-peaks were used in the analysis.

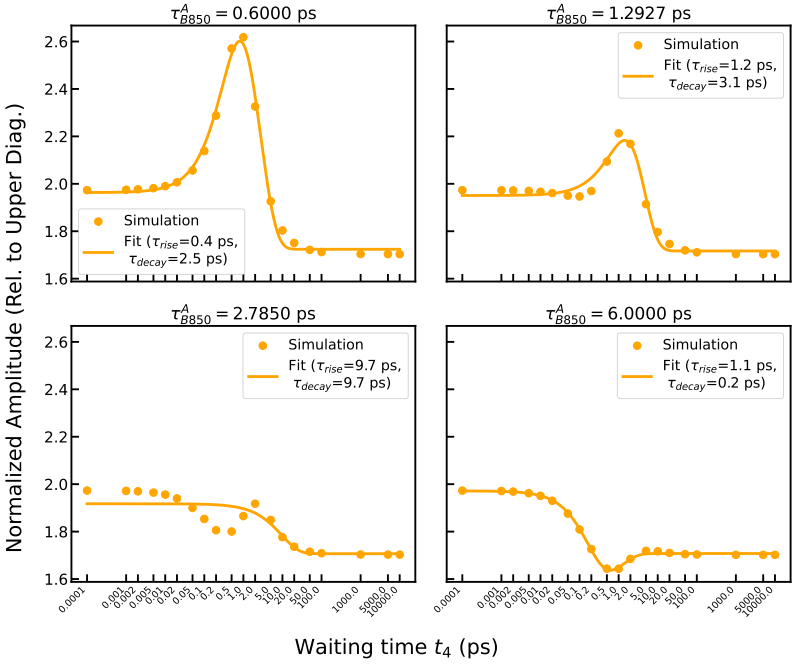

Figure 14: Complex LD behaviour left out of Fig. 12 in the bottom right region. All subplots have $\tau^A_{B800} = 0.0001$ ps.

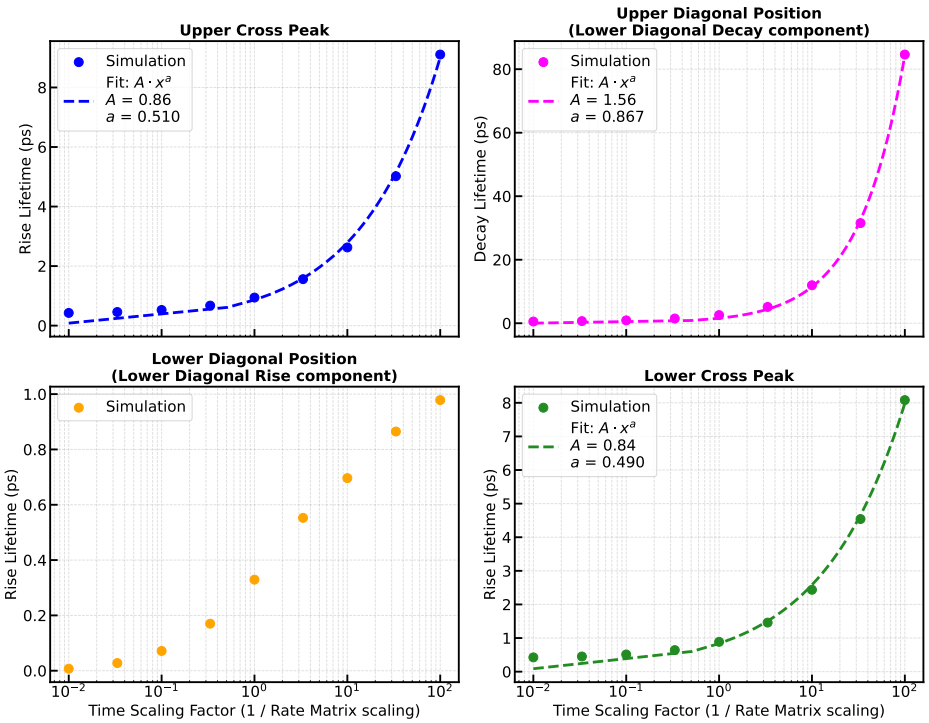

Figure 15: The peak evolution timescales' dependence on the scaling of rate matrix K from Eq. (1). The x-axis is the reciprocal of this scaling to preserve relative dimensions (timescale versus scaling of a timescale). Except for LD, the evolution is fitted with a power fit. Note the logarithmic axes.

effect of scaling K is similar to scaling both annihilation timescales by the same amount. In both cases, the relative contribution of transfer and annihilation is varied. Those two actions do differ, though, mainly in k^F and k^R effects, but also in the stretching of the t_4 axis.

Fig. 15 shows K scaling effect on the four peaks' timescales. The x-axis is reciprocated to represent transfer time scaling, which is more readily comparable to peak timescales. The annihilation parameters were kept at default values, which correspond to a diagonal (bottom left to top right) slice through the 81-parameter spaces in Section 3.3.

The cross-peaks and UD behave as expected, with slower transfer meaning slower peak growth. The effect is much stronger in UD. This is again indicative of most excitons created on B800 having to transfer to B850, where they annihilate. Since the UD has two such excitons, the slowdown due to slower transfer is even stronger than in cross-peaks with only a single exciton needing to transfer.

On the other hand, the lower diagonal rise component is completely non-intuitive. Here, the two excitons are already created in B850, where the majority of the excitations occur. If transfer between segments was slowed down or stopped, the annihilation would be the only thing to eventually happen to those excitons (apart from small radiative and non-radiative components). Allowing faster transfer between segments would let some excitons escape to B800 segments with a very low chance of meeting the second exciton and a comparatively quick decay back to B850. Intuitively, then, the faster the transfer, the more interrupted the B850 annihilation and the slower the signal growth. This would translate to a decreasing bottom left subplot in Fig. 15, where the opposite is observed.

3.5 Limitations and future considerations

3.5.1 General limitations

In the entire preceding analysis, we used four ROIs shaped as squares and centered and scaled manually in a fixed manner. This was done to more clearly quantify the individual peaks' behaviours. It would be just as valid to use more symmetric shapes like circles, or to integrate the entire four quadrants corresponding to the peaks and their surroundings. Alternatively, a smaller shape around the maximum peak could be used to avoid the asymmetric response in Fig. 11b, although this asymmetry can contain information about the Pauli repulsion of the second exciton to be created in B850.

Another general limitation is only focusing on the parallel relative laser pulse polarization. The simulation method allows analysis of all other relative polarizations, which could be explored in a more extensive study for polarization-dependent phenomena. Although this would not impact the incoherent fluorescence during t_4, perhaps a selective exciton population could be created in certain systems.

Lastly, when dealing with exciton population transfer during t_4, multiple excitons are allowed on the same B800 segment, despite it being treated as a two-level system during exciton creation. Also, the rate sub-matrix K is used in K^Q both for its real role, tracking the transfer of a single exciton, and for tracking the transfer between the two-exciton states, assuming the second exciton does not drastically influence this transfer. Both of those assumptions could be challenged in future studies with a more complex simulation method.

3.5.2 Finite t_4 F-2DES

We suggest using a finite t_4 in the standard F-2DES to improve relative signal growth, shown in Fig. 5. But while it may be possible to decrease this detection time cutoff in simulation, there are experimental limitations. Unfortunately, even decreasing this cutoff to 10 ps does not noticeably improve the contrast, requiring significant commitment to shortening it to the EEA timescales to have the desired effect. A further tradeoff is the absolute signal strength, which decreased by at least three orders of magnitude as seen in Fig. 6a. The plots in Fig. 9a can also be interpreted as the absolute signal for $t_2 = 0$ depending on t_4 cutoff, again displaying exponential decrease. If this variation of the F-2DES method is to be realized experimentally, a suitable balance between absolute signal and signal contrast needs to be found, with increasing sample concentration perhaps lightening the burden if possible, sacrificing one of the F-2DES advantages.

3.5.3 Parameter variation impact on experiment

The bulk of the results focuses on the inherent LH2 parameters' influence on the simulated spectral evolution. However, experimentally, only one set of parameters can be measured: the real one. This analysis was then done to find what information about these parameters is contained in the measurement. The transfer rate and B850 annihilation were the main factors, enabling deduction of the LH2 behaviour of aggregating the excitons into the B850 ring. Similar dynamic information is expected to be measurable in other systems, although different fitting models and ROI structures may be necessary. LH2 is a symmetric system with transition rate directionality and only two characteristic frequencies, simplifying this analysis.

Unfortunately, the analytical expressions for the exact fits to the signal, or inherent parameters expressed as a function of these, the fitted ones are impossible due to the high dimensionality of the K^Q matrix (78 dimensions in the 10-segment LH2 example). This is why timescales of simple exponential and bi-exponential fits were used, but different choices could have been made, such as a ratio of two offset exponentials, which showed promise upon brief testing but also introduced more inconsistency.

When varying the annihilation parameters, a special case of no annihilation in either segment type was mostly ignored as an outlier outside the model, but it contains information about ground-state bleach. Unfortunately, the annihilation cannot be turned off experimentally.

3.5.4 UD normalization and the fitting model

While studying raw t_4 dependent data reveals the fluorescent lifetime $\tau^F \approx 986$ ps, elucidating the transfer and annihilation dynamics of excitons evolving within the system requires removing this overarching signal growth. Since experimentally the exact τ^F would not be known, we normalized all peak signals by the upper diagonal. This imprints the UD evolution onto all peaks, most readily seen in LD, from where it is interpreted. The bi-exponential fit here does not yield the same presumed UD timescale as a ratio-of-exponentials fit would, a seemingly more reasonable model. However, fitting the cross peaks with a ratio does not reproduce the same denominator as LD, and also indicates the UD signal would decay with time. This confirms that a proper fit is more complicated than a ratio of two exponentials, so a more stable bi-exponential was chosen here. The likely reason why cross-peaks did not exhibit the same rising and falling dynamics as LD is that both cross-peaks and UD require transfer of excitons from B800 to B850. Because UD requires two of those transfers, the main trend observed in normalized cross-peaks is the result of partial cancellation of those identical dynamics. LD signal comes mainly from the immediate annihilation of excitons already on B850, leading to no cancellation and a more complicated composition of those two signals after normalization. Of course, parts of the signal come from B800 annihilation too, which differ between the peaks, even cross-peaks and UD, possibly causing the fall and rise dynamics in Fig. 11b.

4 Conclusions

Fluorescence-detected Two-Dimensional Electronic Spectroscopy (F-2DES) enables a background-free measurement of correlations between excitation frequencies in a molecular system. After two excitons are created using four laser pulses, they hop between molecules and decay with or without emitting a photon. By measuring the photons, a Two-Dimensional (2D) spectrum is obtained for each waiting time t_2 between the two exciton-creating pulse pairs. The spectrum shows the non-linear difference from the independent excitons' signal, as a function of the two excitation frequencies. Of main interest are the cross-peaks, correlations between different exciton frequencies. Unfortunately, these are obscured in F-2DES due to Exciton-Exciton Annihilation (EEA) that non-radiatively de-excites one exciton if they are in close proximity. This is because the incoherent photons are measured for a long time after the last pulse, meaning all of the excitons' hopping and annihilation signal gets integrated, leaving a large cross-peak with minimal variation throughout t_2 scanning.

Here, we have shown that measuring the fluorescent photons only until a shorter cutoff time t_4 after the last pulse increases the contrast between 2D spectra at different t_2 waiting times. A tradeoff for this is a lower absolute signal (number of photons detected). This means that there is a freedom to optimize between those two aspects in an experimental realization to improve the contrast over regular F-2DES with effectively infinite t_4. Unfortunately, the decrease of t_4 towards the annihilation time-scale's magnitude may be necessary, which is around 0.1 ps for the studied LH2 system (Light Harvesting complex 2 of purple bacteria *R. acidophilus*).

The quantum yield ratio, the average expected number of photons emitted per pair of excitons over those emitted per one exciton, changes in t_4 due to EEA. Because both types of quantum yields scale parts of the signal, the signal's dependence on t_4 deviates from a uniform growth, containing information about EEA and exciton hopping. This can be used in a novel method explored here: time-resolved F-2DES, where t_2 is fixed, and a t_4 dependent signal is measured. We found that the raw signal recovers the inherent fluorescent timescale τ^F, here 986 ps. To find the deviations from this uniform growth, we normalized by the Upper Diagonal (UD) peak's integrated signal. The resulting normalized signal shows growth due to exciton hopping and annihilation at timescales of $0.4 - 2.1$ ps, close to the known timescales used for the simulation. The behaviour of UD was also deduced from a decay it introduced in the Lower Diagonal (LD) peak. Overall, the peaks' behaviours indicated the known dynamics in LH2 of excitons hopping almost unidirectionally from B800 chromophores to the B850 chromophore ring.

To determine what information is contained in the normalized peak evolutions, those were compared for a set of annihilation parameter combinations, including ultra-fast and ultra-slow annihilation regimes. Consistently, the B850 annihilation rate was found to influence the normalized peak evolution much more drastically than the B800 rate (changing the order of magnitude versus changing by 10%). This makes sense, knowing the above-mentioned general behaviour, but remains inaccessible experimentally. While the annihilation timescale cannot be directly read off from the normalized peak evolutions, modeling and regression could inform the parameter, likely only if other degrees of freedom were fixed, such as (non)radiative exciton decay rates and the transfer rates between molecular segments.

Specifically, the transfer rate effect on the normalized peak evolution was also explored here. The transfer rate matrix K from MC-FRET was scaled by a constant factor, preserving the

relative hopping rates. The resulting peak evolution timescales grew or shrank as expected by the B800 to B850 net transfer, except for the LD region. The behavior is opposite to the intuitive explanation, suggesting either a limitation in peak evolution timescales' interpretation or the fitting procedure.

Overall, this novel method promises to improve the standard F-2DES signal contrast, but also provides access to more information about exciton dynamics. This study only examined slices of the multi-dimensional parameter space, paving the way for further exploration. Varying laser pulse polarization, (non)radiative exciton decay rates, and varying both t_2 and t_4 are all many-dimensional extensions of the current study. More comprehensively, improving fitting models and including the effects of two excitons on their hopping could benefit all further parameter explorations. This may eventually enable harvesting approximate internal exciton dynamics information purely from regression on time-resolved F-2DES data.

Bibliography

[1] T. Brixner, J. Stenger, H. M. Vaswani, M. Cho, R. E. Blankenship, and G. R. Fleming, "Two-dimensional spectroscopy of electronic couplings in photosynthesis," *Nature*, vol. 434, no. 7033, pp. 625–628, Mar 2005.

[2] P. Hamm, M. Lim, and R. M. Hochstrasser, "Structure of the amide i band of peptides measured by femtosecond nonlinear-infrared spectroscopy," *The Journal of Physical Chemistry B*, vol. 102, no. 31, pp. 6123–6138, Jul 1998.

[3] R. B. Woodward, "Structure and the absorption spectra of α,β-Unsaturated Ketones," *Journal of the American Chemical Society*, vol. 63, no. 4, pp. 1123–1126, 1941.

[4] W. M. Zhang, V. Chernyak, and S. Mukamel, "Multidimensional femtosecond correlation spectroscopies of electronic and vibrational excitons," *The Journal of Chemical Physics*, vol. 110, no. 11, pp. 5011–5028, 1999.

[5] W. P. Aue, E. Bartholdi, and R. R. Ernst, "Two-dimensional spectroscopy. Application to nuclear magnetic resonance," *The Journal of Chemical Physics*, vol. 64, no. 5, pp. 2229–2247, 1976.

[6] J. D. Hybl, A. W. Albrecht, S. M. Gallagher Faeder, and D. M. Jonas, "Two-dimensional electronic spectroscopy," *Chemical Physics Letters*, vol. 297, no. 3-4, pp. 307–313, 1998.

[7] D. M. Jonas, "Two-dimensional femtosecond spectroscopy," *Annual Review of Physical Chemistry*, vol. 54, no. 1, pp. 425–463, 2003.

[8] P. Tian, D. Keusters, Y. Suzaki, and W. S. Warren, "Femtosecond phase-coherent two-dimensional spectroscopy," *Science*, vol. 300, no. 5625, pp. 1553–1555, 2003.

[9] K. J. Karki, J. R. Widom, J. Seibt, I. Moody, M. C. Lonergan, T. Pullerits, and A. H. Marcus, "Coherent two-dimensional photocurrent spectroscopy in a pbs quantum dot photocell," *Nature Communications*, vol. 5, no. 1, p. 5869, 2014.

[10] S. Jana, S. Durst, and M. Lippitz, "Fluorescence-detected two-dimensional electronic spectroscopy of a single molecule," *Nano Letters*, vol. 24, no. 40, pp. 12 576–12 581, 2024.

[11] P. Malý and T. Brixner, "Fluorescence-detected pumpprobe spectroscopy," *Angewandte Chemie International Edition*, vol. 60, no. 34, pp. 18 867–18 875, 2021.

[12] S. Goetz, D. Li, V. Kolb, J. Pflaum, and T. Brixner, "Coherent two-dimensional fluorescence micro-spectroscopy," *Optics Express*, vol. 26, no. 4, pp. 3915–3925, 2018.

[13] S. Gonzalez-Migoni and T. L. C. Jansen, "Fluorescence-detected two-dimensional electronic spectroscopy: A coarse-grained simulation approach," *The Journal of Chemical Physics*, vol. 164, no. 10, p. 104112, 2026.

[14] T. Kunsel, V. Tiwari, Y. Acosta Matutes, A. T. Gardiner, R. J. Cogdell, J. P. Ogilvie, and T. L. C. Jansen, "Simulating fluorescence-detected two-dimensional electronic spectroscopy of multichromophoric systems," *The Journal of Physical Chemistry B*, vol. 123, no. 1, pp. 394–405, 2019.

[15] H. Lemmetyinen, N. V. Tkachenko, B. Valeur, J.-i. Hotta, M. Ameloot, N. P. Ernsting, T. Gustavsson, and N. Boens, "Time-resolved fluorescence methods (iupac technical report)," *Pure and Applied Chemistry*, vol. 86, no. 12, pp. 1969–1998, 2014.

[16] T. l. C. Jansen, *Ultrafast Dynamics and Multi-dimensional Spectroscopy*. Groningen, The Netherlands: University of Groningen, 2020, lecture notes for the Ultrafast Dynamics course, Zernike Institute for Advanced Materials.

[17] P. F. Tekavec, G. A. Lott, and A. H. Marcus, "Fluorescence-detected two-dimensional electronic coherence spectroscopy by acousto-optic phase modulation," *The Journal of Chemical Physics*, vol. 127, no. 21, p. 214307, 2007.

[18] K. Zhong, H. L. Nguyen, T. N. Do, H.-S. Tan, J. Knoester, and T. L. C. Jansen, "Coarse-grained approach to simulate signatures of excitation energy transfer in two-dimensional electronic spectroscopy of large molecular systems," *Journal of Chemical Theory and Computation*, vol. 20, no. 14, pp. 6111–6124, 2024.

[19] H. van Amerongen, L. Valkunas, and R. van Grondelle, *Photosynthetic Excitons*. Singapore: World Scientific, 2000.

[20] K. Zhong, H. L. Nguyen, T. N. Do, H.-S. Tan, J. Knoester, and T. L. C. Jansen, "An efficient time-domain implementation of the multichromophoric förster resonant energy transfer method," *The Journal of Chemical Physics*, vol. 158, no. 6, p. 064103, 2023.

[21] T. D. Goddard, C. C. Huang, E. C. Meng, E. F. Pettersen, G. S. Couch, J. H. Morris, and T. E. Ferrin, "Ucsf chimerax: Meeting modern challenges in visualization and analysis," *Protein Science*, vol. 27, no. 1, pp. 14–25, 2018.

[22] Y. J. Yan, L. E. Fried, and S. Mukamel, "Ultrafast pump-probe spectroscopy: femtosecond dynamics in liouville space," *The Journal of Physical Chemistry*, vol. 93, no. 25, pp. 8149–8162, 1989.

[23] R. M. Hochstrasser, "Two-dimensional ir-spectroscopy: polarization anisotropy effects," *Chemical Physics*, vol. 266, pp. 273–284, 2001.

[24] T. L. C. Jansen *et al.*, "NISE_2017: A quantum classical package for calculating coherent multidimensional spectra," https://github.com/GHlacour/NISE_2017, 2017.

[25] R. Monshouwer, M. Abrahamsson, F. van Mourik, and R. van Grondelle, "Superradiance and exciton delocalization in bacterial photosynthetic light-harvesting systems," *The Journal of Physical Chemistry B*, vol. 101, no. 37, pp. 7241–7248, 1997.

[26] G. Trinkunas, J. L. Herek, T. Polívka, V. Sundström, and T. Pullerits, "Exciton delocalization probed by excitation annihilation in the light-harvesting antenna LH2," *Physical Review Letters*, vol. 86, no. 18, pp. 4167–4170, 2001.